


Calibration by differentiation – Self-supervised calibration for X-ray microscopy using a differentiable cone-beam reconstruction operator

Mareike Thies¹  | Fabian Wagner¹ | Yixing Huang¹ | Mingxuan Gu¹ | Lasse Kling² | Sabrina Pechmann³ | Oliver Aust⁴ | Anika Grüneboom⁵ | Georg Schett^{4,6} | Silke Christiansen^{2,3,7} | Andreas Maier¹

¹Pattern Recognition Lab, Friedrich-Alexander-Universität Erlangen-Nürnberg, Erlangen, Germany

²Institute for Nanotechnology and Correlative Microscopy e.V. INAM, Forchheim, Germany

³Fraunhofer Institute for Ceramic Technologies and Systems IKTS, Forchheim, Germany

⁴Department of Internal Medicine 3 – Rheumatology and Immunology, Friedrich-Alexander-Universität Erlangen-Nürnberg and Universitätsklinikum Erlangen, Erlangen, Germany

⁵Leibniz Institute for Analytical Sciences ISAS, Dortmund, Germany

⁶Deutsches Zentrum für Immuntherapie, Friedrich-Alexander-Universität Erlangen-Nürnberg and Universitätsklinikum Erlangen, Erlangen, Germany

⁷Physics Department, Freie Universität Berlin, Berlin, Germany

Correspondence

Mareike Thies, Pattern Recognition Lab, Friedrich-Alexander-Universität Erlangen-Nürnberg, Erlangen, Germany. Email: mareike.thies@fau.de

Funding information

European Research Council, European Union's Horizon 2020 Research and Innovation Programme, Grant No. 810316

Abstract

High-resolution X-ray microscopy (XRM) is gaining interest for biological investigations of extremely small-scale structures. XRM imaging of bones in living mice could provide new insights into the emergence and treatment of osteoporosis by observing osteocyte lacunae, which are holes in the bone of few micrometres in size. Imaging living animals at that resolution, however, is extremely challenging and requires very sophisticated data processing converting the raw XRM detector output into reconstructed images. This paper presents an open-source, differentiable reconstruction pipeline for XRM data which analytically computes the final image from the raw measurements. In contrast to most proprietary reconstruction software, it offers the user full control over each processing step and, additionally, makes the entire pipeline deep learning compatible by ensuring differentiability. This allows fitting trainable modules both before and after the actual reconstruction step in a purely data-driven way using the gradient-based optimizers of common deep learning frameworks. The value of such differentiability is demonstrated by calibrating the parameters of a simple cupping correction module operating on the raw projection images using only a self-supervisory quality metric based on the reconstructed volume and no further calibration measurements. The retrospective calibration directly improves image quality as it avoids cupping artefacts and decreases the difference in grey values between outer and inner bone by 68–94%. Furthermore, it makes the reconstruction process entirely independent of the XRM manufacturer and paves the way to explore modern deep learning reconstruction methods for arbitrary XRM and, potentially, other flat-panel computed tomography systems. This exemplifies how differentiable reconstruction can be leveraged in the context of XRM and, hence, is an important step towards the goal of reducing the resolution limit of in vivo bone imaging to the single micrometre domain.

This is an open access article under the terms of the [Creative Commons Attribution](https://creativecommons.org/licenses/by/4.0/) License, which permits use, distribution and reproduction in any medium, provided the original work is properly cited.

© 2022 The Authors. *Journal of Microscopy* published by John Wiley & Sons Ltd on behalf of Royal Microscopical Society.

KEYWORDS

computed tomography, deep learning, inverse problems, known operator learning, reconstruction, X-ray microscopy

1 | INTRODUCTION

Dedicated imaging is required to investigate malfunctions in bone remodelling, which manifest themselves in diseases like osteoporosis. The very small-scale structures in bones play an important role in the process of bone build-up and decrease.¹ In particular, osteocytes are known to orchestrate bone remodelling.² These cells are located in ellipsoidal holes in the bone, the lacunae, which have been quantified to have a size of 3–20 μm ³ (recent findings even suggest that the upper end of this range reflects small transcortical vessels instead of lacunae⁴). However, their exact role in pathological changes of bone structure such as osteoporosis is still poorly understood.⁵ A central reason for this is that all imaging technologies capable of resolving structures at a scale of few micrometres can currently only be applied to *ex vivo* samples.^{2,6–9} Such experiments cannot reveal any longitudinal relationship between the progression of osteoporosis and changes in the bony microstructure. *in vivo* measurements of animal bones could reveal those insights but are currently limited to around 20–50 μm resolution which is not sufficient to reliably resolve the lacunae.^{10,11} A promising technology for pushing this *in vivo* limit towards the single micrometre domain is X-ray microscopy (XRM), which is non-destructive and achieves a high contrast between bone and soft tissue. Such data would be of great value to broaden the understanding of osteoporosis.

Several challenges currently hinder the application of XRM to *in vivo* samples. These are concerns about the X-ray dose deposited in the animal, sample motion due to respiration or heartbeat of the animal, and insufficient calibration of the XRM to biological samples.^{12,13} These issues need to be addressed before any experiments with living animals can be performed. A severely degraded image quality is to be expected otherwise. Addressing these challenges demands for sophisticated data processing beyond post-processing of the reconstruction obtained from the scanner but incorporating both raw projection data and reconstructed images. Such algorithms would ideally intervene at multiple stages of the data processing pipeline converting the raw XRM detector output into reconstructed images. However, such an algorithmic approach is currently not possible because the reconstruction and data processing is usually implemented as proprietary software with limited user control directly on the scanner which outputs a reconstructed image but is

essentially a black box for the operator. Hence, to proceed on the path towards *in vivo* imaging, it is crucial to open that black box in order to adapt and augment the data processing pipeline exactly to the given use case.

This paper presents an open-source implementation of an entire reconstruction pipeline from the raw measurement data of a Zeiss XRM scanner. It includes the loading of projection data from the proprietary file format, extraction of the scan geometry information, necessary correction and preprocessing steps on the projection images and a filtered back-projection in the correct geometry to analytically invert the XRM measurement process. Not only does this allow for fully controlled data processing without any dependency on proprietary software, but the implementation is also differentiable, thereby making the entire pipeline deep learning compatible. This is an important step towards any experiment including living animals because it is a tool that enables the user to freely change and adapt each step in the pipeline and, most importantly, to augment it with state-of-the-art learning-based approaches.

Based on this pipeline, we present a dual-domain approach to the problem of cupping correction because we find that cupping artefacts are a prominent deterioration of image quality in our current XRM measurements making downstream tasks such as lacunae segmentation unnecessarily difficult. Instead of learning the parameters of a deep model, we calibrate just the very few (2–3) free parameters of a cupping correction step using only the corrupted data itself and with no additional phantom measurements needed. This is possible because a self-supervised target function can be formulated directly on the reconstructed volume while still driving parameter updates in the raw data domain. The cupping correction is a simple yet effective application of the proposed reconstruction pipeline which also hints at its potential in tasks requiring deeper models like complex artefact suppression^{14,15} or image denoising.^{16,17}

In summary, the main contributions of this paper are:

1. For the raw projection data acquired on a Zeiss X-ray microscope, we translate the unstructured metadata and image information into a well-defined format which can directly be used with any state-of-the-art cone-beam computed tomography (CBCT) reconstruction framework. The raw geometry information is converted to universal and widely used projection matrices

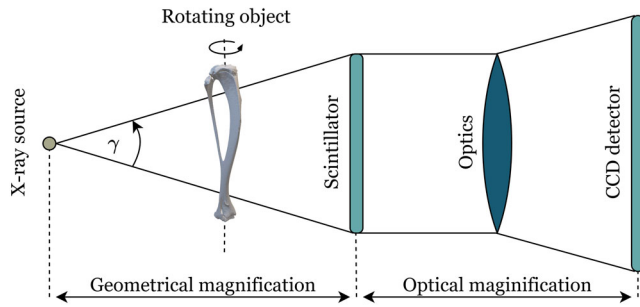


FIG 1 X-ray microscopy couples the geometrical magnification of a cone-beam CT setup with further optical magnification to capture extremely high-resolution projection images

which are the most general representation of a 3D scan geometry. Projection images are pre-processed and made ready for reconstruction.

- From the available open-source CBCT reconstruction frameworks, we specifically choose a differentiable algorithm that allows for automatic gradient-based optimization of free parameters – for classical optimization problems or in a deep learning sense – across the reconstruction operator without the need to manually compute the gradient.
- We demonstrate the usefulness of such differentiability by fitting a low-dimensional cupping correction model both on a per-scan basis and on a full data set of murine tibia XRM scans divided into training and test data.
- The code and example data are made publicly available.

2 | MATERIALS AND METHODS

2.1 | X-ray microscopy

XRM is applied in a range of different research disciplines, among them are material science, geoscience and life science.^{18–21} Depending on the application, the exact type of microscope can differ in a number of aspects, such as the source properties or the scanning procedure. The basic working principle of the system deployed in this study is similar to classical CBCT, but it deploys an additional optical system which further increases the resolution. A polychromatic X-ray source with a low spot size generates cone-shaped, divergent X-ray beams which traverse the object and lead to geometrical magnification. A scintillator converts the X-ray photons into visible light which is coupled into an optical system for further magnification and detected by a charge-coupled device (CCD) camera (see Figure 1). On their way to the detector, the X-ray photons are attenuated depending on the properties of the material they traverse. Hence, the pixel values in the measured

TABLE 1 XRM scan settings

X-ray source voltage	60 kVp
X-ray source current	108 μ A
Number of acquired projection images per scan	1401
Angular range	202° (short scan)
Exposure time per projection	28 s
Detector shape	2038 \times 2038
Detector pixel size	11.0 μ m
Source–isocentre distance	10.3 mm
Isocentre–detector distance	10.0 mm
Magnification (geometrical/optical/total)	1.97/4/7.88
Reconstructed volume shape (height \times width \times slices)	1997 \times 2038 \times 2014
Voxel size	1.4 μ m
Spatial resolution	2.5 μ m
Signal-to-noise ratio	57.1

2D projection images depend on the integral of the entire attenuation that the photon has experienced on the ray between source and detector pixel. X-ray projection images are acquired from multiple angles by rotating the sample around its vertical axis. To sample each ray through the central horizontal plane of the object at least once, a rotation of at least 180° plus the fan angle γ is required (short scan).

For our experiments, we use an ex vivo murine tibia data set. It consists of eight scans of the most distal part of the tibia which forms part of the animal's ankle. Exemplary centre slices are depicted in the first column of Figure 4. The data set is acquired on a Zeiss Xradia 620 Versa microscope (Carl Zeiss) with a tube current of 108 μ A and a source voltage of 60 kV which accelerates electrons towards a tungsten transmission anode. The resulting X-ray spectrum has a maximum energy of 60 keV. The X-rays pass an additional spectral filter after which the exact X-ray spectrum is unknown. Other scan parameters are summarized in Table 1. The voxel size of 1.4 μ m corresponds to the pixel size of the detector when virtually scaled to the isocentre, that is, the quotient of physical detector pixel size and total magnification. The spatial resolution inferred from measurements of a stripe pattern phantom is 2.5 μ m (see Figure 1 in the supplementary material). The signal-to-noise ratio is computed as the quotient of the mean bone grey value and the standard deviation of the grey values in a background patch on the centre slice of one scan reconstructed by the proprietary software. Note that all scan parameters are optimized for high-resolution imaging of ex vivo samples and are not directly transferable to in vivo samples.

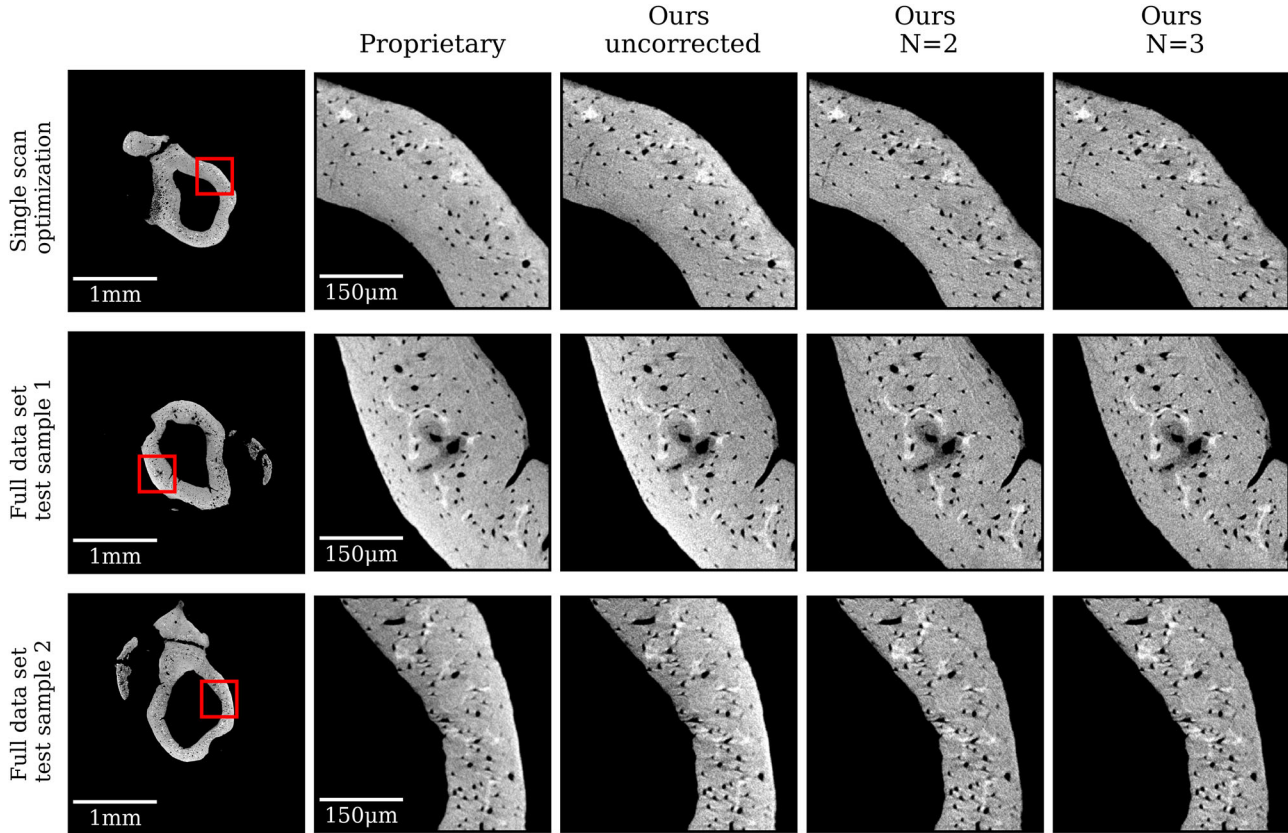


FIG 4 Qualitative reconstruction results comparing centre slices of the proprietary algorithm with our proposed algorithm. We show the results without any cupping correction applied and after performing a cupping correction with a polynomial of degree $N = 2$ and $N = 3$. The first row is a result of a per-sample optimization whereas rows two and three show the results of the two test samples from the full data set experiment. The proprietary and the uncorrected reconstruction using our pipeline exhibit brighter grey values at the outer border of the bone. This effect is largely removed in the corrected versions. All figures have a grey value window of 900–2300 HU

2.2 | Ethical compliance and sample preparation

We complied with all relevant ethical regulations in terms of organ removals in this study. All organ removals conducted at the University of Erlangen were performed in accordance with German guidelines and laws, were approved by local animal ethic committees of the Regierung von Mittelfranken (TS-12/2015), and were conducted according to the guidelines of the Federation of European Laboratory Animal Science Associations. In this study, C57BL/6 mice of both sexes were used. The mice were aged 56–93 weeks. For sample preparation, the mice were euthanized by CO₂, perfused with 5 mM EDTA/PBS, and perfusion-fixed with 4% PFA/PBS (pH 7.4). Tibiae were relieved from muscle tissue and post-fixed in 4% PFA/PBS (pH 7.4) for 4 h at 4–8°C with gentle shaking. Tissue fixation was followed by 100% ethanol dehydration. The ethanol-dehydrated bones were then transferred to the XRM.

2.3 | Differentiable cone-beam reconstruction

CBCT reconstruction seeks to invert the mathematical forward model of X-ray image formation characterized by the integration of attenuation coefficients along rays through the volume according to the Lambert–Beer law. The measured detector signal is a series of 2D projection images of the volume along rays defined by the imaging geometry and is referred to as sinogram. This signal is translated back into a 3D volume in image space by a reconstruction algorithm. An analytical, approximate and widely used filtered-back-projection CT reconstruction algorithm for cone-beam geometry is known as Feldkamp–Davis–Kress (FDK) reconstruction.²² It comprises a scaling of projection images by a cosine function, a row-wise filtering of projection images with a ramp filter in Fourier domain and a back-projection of filtered projection images along rays through the volume weighted by the distance between the reconstruction and the focal point. We refer the reader

to Ref. 23 for a detailed explanation of this algorithm. For short scan acquisitions ($180^\circ + \gamma$ trajectories instead of a full 360° rotation), an additional Parker weighting is used to downweigh oversampled rays.²⁴

It has been shown that CT reconstruction can be regarded as a differentiable operation, meaning that the partial derivative of each output voxel with respect to each projection pixel in the input can be calculated. Consequently, the back-projection algorithm can be embedded as a known operator within a neural network.²⁵ As such, it does not contain any trainable parameters on its own but introduces analytical knowledge about the reconstruction step into a differentiable computation graph. This graph connects it via the chain rule of differentiation to potential other trainable modules in both sinogram and image domain, that is, before or after the reconstruction step, respectively. The differentiability ensures that a gradient of a loss function in image domain can flow back into the sinogram domain. This is required to update trainable weights operating in both domains in an end-to-end fashion using standard gradient-based optimization which drives the training of neural networks. Most well-known open-source CBCT reconstruction frameworks are not differentiable out-of-the-box. Some works consequently deploy a wrapper²⁶ around such non-differentiable frameworks like the ASTRA toolbox²⁷ or *TomoPy*²⁸ which allows for integration into differentiable pipelines. Other frameworks are tailored specifically towards differentiability.^{29,30} A detailed comparison of these different implementations is beyond the scope of this work. We use the *PyroNN* framework by Syben et al.²⁹ for all following investigations as it is a computationally efficient solution for differentiable CT reconstruction modules which are integrated into the recent deep learning frameworks. It allows using the said reconstruction module in conjunction with the automatic differentiation algorithms which drive the parameter updates in common deep learning frameworks. The user only specifies the forward model and optimization via gradient descent is performed automatically, iteratively approaching a locally minimal solution with respect to the calculated loss function. In this work, we build upon that framework wrapped for the deep learning framework *PyTorch*³¹ to implement the reconstruction for the XRM data.

The embedding of knowledge about the physics underlying CT reconstruction into learned pipelines has been explored before, mostly in the medical context, but also on XRM data similar to ours.^{32–34} The areas of application range from improving reconstruction quality in low dose, limited or missing angle scenarios^{34,35} over learning of data-optimal reconstruction filters or weights^{36,37} to calibration of, for example, the position of the rotation axis from the measured data.³² Some of the mentioned approaches propose deep learning architectures in the

classical sense involving a high number of trainable parameters. However, as prior knowledge is explicitly imposed by the reconstruction operator, it is often possible to reduce the number of free parameters considerably.²⁵ In the extreme cases, only a small number of free parameters which have a well-defined task suffice to model the problem in an interpretable way. Training these very low parametric methods could be viewed as general gradient-based optimization. Nevertheless, they still rely on the automatic differentiation of frameworks like *PyTorch* which bypasses the non-trivial work to manually compute the corresponding gradient. Just as for classical deep learning approaches, defining the forward model suffices making a clear distinction between deep learning and mere optimization methods in the context of differentiable reconstruction operators difficult.

2.4 | Details on reconstruction pipeline

The proposed reconstruction pipeline consists of several steps highlighted as coloured boxes in Figure 2. Input to the pipeline is the raw measurement data from the scanner stored in a proprietary file format (*.txrm*). One such file contains all projection images of a scan as well as metadata concerning the geometry or correction factors. Our reader is extended from work by De Carlo et al.³⁸ and extracts images and the necessary header information. Next, several pre-processing steps are performed on the raw projection images. These are a flat field correction and a revision of detector shifts which are applied intentionally during data acquisition to minimize the influence of defect pixels on the detector. Following these steps, by applying the negative logarithm, the projection data are converted to line integral domain which reflects the actual attenuation instead of the remaining X-ray intensity after traversing the object. Finally, a truncation correction is applied if the imaged object exceeds the detector. The projection images are laterally extended by 10% of the original image width on both left and right sides and the imaged bone is extrapolated by linearly fading out absorption values to zero towards both sides. To cope with the high memory requirements of the given data, downsampling can be applied both spatially and in angular direction. The scan's geometry is defined in terms of projection matrices. These define the geometrical relationship of 3D points in the volume and their corresponding detector location after projection under a given angle. An ideal circular trajectory is assumed and specified by the following parameters from the metadata: The number of projection images, their primary acquisition angles, the detector height and width in pixels, the detector pixel size, the source to rotation centre distance, the detector offset from the centre and the cone angle. Given the pre-processed projection images and their

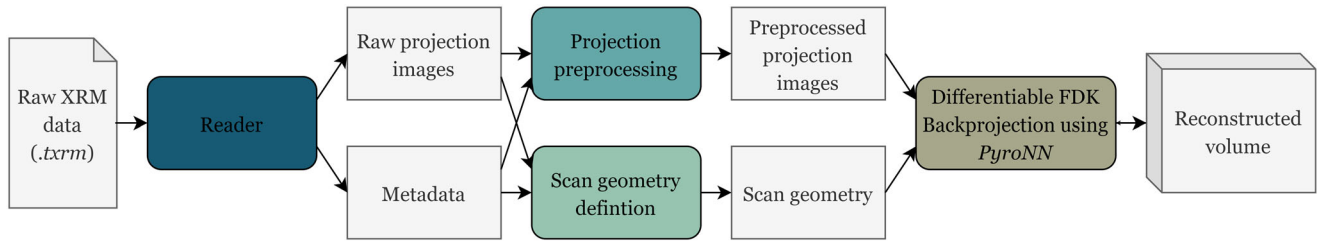


FIG 2 Overview of the proposed reconstruction pipeline. We implement each of the coloured boxes to (1) read the raw projection data, (2) pre-process the images, (3) define the scan geometry and (4) perform a filtered back-projection

corresponding projection matrices, the differentiable back-projection module introduced in the previous section is called. It performs the Parker and cosine weighting, ramp filtering and actual back-projection into the volume based on the differentiable implementation in Ref. 29. The final reconstruction represents the spatial function of attenuation values which are typically given in Hounsfield Units (HU), where the attenuation of water corresponds to 0 HU and the attenuation of air is -1000 HU.³⁹ As such, our pipeline does not contain any trainable parameters at all. Rather, we see it as a tool that can enable state-of-the-art reconstruction approaches for Zeiss XRM data. In Section 2.5, we propose a simple application of the pipeline in the context of mouse bone imaging.

2.5 | Application to cupping correction

CT reconstruction algorithms usually neglect the fact that the attenuation of X-rays traversing an object is not only material- but also energy-dependent. In reality, however, lower-energetic parts of the X-ray spectrum are typically attenuated stronger than high-energetic parts, especially in dense material like bone. This introduces a non-linear error in the detector signal leading to cupping artefacts or dark streaks in the reconstruction.^{40,41} We observe those cupping artefacts in the data reconstructed by our pipeline and in the proprietary reconstruction in the form of decreasing grey values of the bone towards the bone marrow (see Figure 4, ‘Ours uncorrected’). As cupping artefacts arise from a distortion of grey values in the projection images, they can effectively be reduced by a correction polynomial of degree N

$$\hat{x}(\mathbf{c}) = \sum_{n=1}^N c_n x^n, \quad c_n \in \mathbb{R}, \quad (1)$$

which maps each grey value x to its corrected value \hat{x} in projection domain. This polynomial contains N scanner- and object-dependent parameters stored in the vector $\mathbf{c} \in \mathbb{R}^N$. These can, for example, be found via calibration with a known phantom⁴² or by maximizing the consis-

tency between the projection images.⁴³ With the proposed framework, the fitting of the free polynomial coefficients can be achieved easily by including the polynomial mapping in Equation (1) into the differentiable computation graph before feeding the projection images to the back-projection module (see Figure 3). Only the coefficients \mathbf{c} of the polynomial in Equation (1) are defined as trainable parameters within *PyTorch*. Because image and projection domain are connected in a differentiable way, the target function for optimizing the coefficients can be formulated in image domain and still drive the updates of \mathbf{c} operating in projection domain. More precisely, the projection images are first corrected by the polynomial cupping correction model with trainable parameters \mathbf{c} and then reconstructed using the differentiable framework *PyroNN* which performs Parker and cosine weighting, ramp filtering and the actual back-projection operation (see Section 2.3). The obtained reconstruction is normalized to unit standard deviation and a self-supervised loss in the form of the total variation (TV) norm is applied. Because each step in this chain is differentiable, the gradient of the TV norm can be propagated backwards such that it can finally be used to update \mathbf{c} . The TV loss is defined as

$$\text{TV}(\mathbf{I}) = \sum_{j=0}^J |\nabla I_j|_1. \quad (2)$$

It integrates the absolute values of the image gradient ∇I for all pixels j thereby preferring piecewise constant solutions. Our intuition behind choosing the TV norm as a loss function is that this function punishes intensity gradients such as those introduced by beam hardening.

When left unconstrained, the self-supervised optimization of \mathbf{c} could converge towards trivial solutions, for example, $\mathbf{c} = \mathbf{0}$. To restrict this effect, we enforce that the coefficients \mathbf{c} have unit ℓ_2 -norm with

$$\|\mathbf{c}\|_2 = 1. \quad (3)$$

Incorporating this constraint into the gradient-based optimization requires restricting the space of possible solutions for the free parameters \mathbf{c} . All gradient updates on \mathbf{c} must

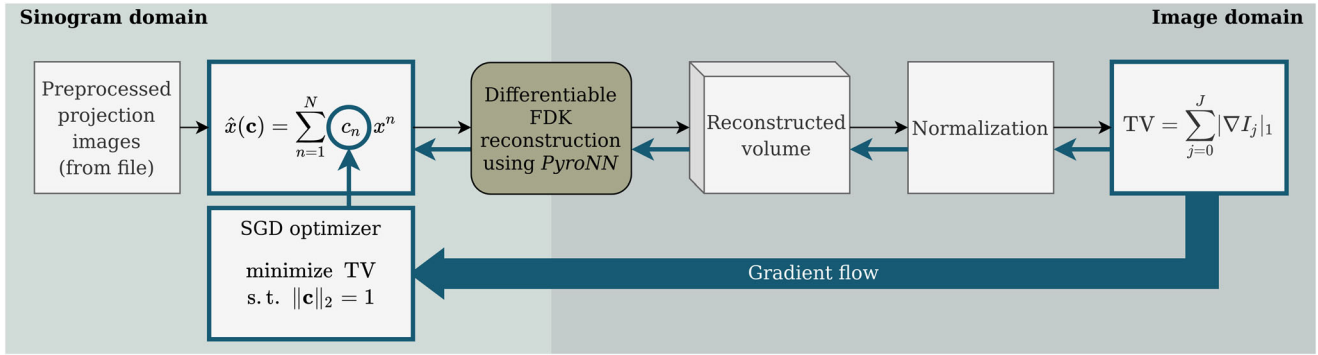


FIG 3 Self-supervised calibration of a polynomial mapping for cupping correction. The forward model of the correction step is specified and inserted into the differentiable computation graph in sinogram domain. A TV norm on the reconstructed volume serves as objective function for automatic gradient-based optimization of the free parameters $\mathbf{c} \in \mathbb{R}^N$ with $N \in \{2, 3\}$

still fulfil Equation (3) and hence lead to solutions which lie on the N -dimensional unit sphere with respect to the ℓ_2 -norm. Such update steps can be performed using special Riemannian optimizers. Gradients are computed in the tangent space of the current location on the manifold of the N -dimensional unit sphere and the optimizer performs a special gradient update which cannot leave the manifold.^{44,45} We use the Riemannian version of the well-known stochastic gradient descent (SGD) optimizer with a learning rate of 10^{-9} which ensures that the required constraint in Equation (3) is always fulfilled. A pseudo-code formulation of the proposed cupping correction algorithm is given in Algorithm 1.

3 | EXPERIMENTS

We perform two types of experiments:

1. Per-scan experiments: Cupping correction is performed on a per-scan basis where the polynomial parameters \mathbf{c} are optimized on the target scan itself.
2. Full data set experiments: Cupping correction is performed on a full data set split into training, validation and test samples. One parameter vector \mathbf{c} is fitted using all training samples and applied without changes to correct previously unseen test samples.

In the second case, we split the eight available bone scans into five samples for training, one for validation and two for

Algorithm 1 Self-supervised cupping correction

```

input      : projection images in line-integral domain  $\mathbf{x}$ 
              scan geometry as projection matrices  $\mathbf{p}$ 
parameters: degree of the polynomial  $N$ 
              learning rate  $\mu$ 
              number of epochs  $M$ 
output    : optimized polynomial parameter vector  $\mathbf{c}^*$ 
init  $\mathbf{c}_1^{(0)} \leftarrow 1, \mathbf{c}_{2:N}^{(0)} \leftarrow 0$ 
for  $i = 0$  to  $M - 1$  do
     $\hat{\mathbf{x}}(\mathbf{c}^{(i)}) = \sum_{n=1}^N c_n^{(i)} \mathbf{x}^n$  // apply polynomial
     $\mathbf{r} = \text{FDK}(\hat{\mathbf{x}}, \mathbf{p})$  // compute FDK reconstruction
     $\hat{\mathbf{r}} = \mathbf{r} / \text{std}(\mathbf{r})$  // normalize reconstruction
     $L = \text{TV}(\hat{\mathbf{r}})$  // compute TV-loss to be minimized
     $\frac{\partial L}{\partial \mathbf{c}} = L.\text{backward}()$  // PyTorch-specific command for automatic gradient computation
     $\mathbf{c}^{(i+1)} = \text{SGD}(\mathbf{c}^{(i)}, \frac{\partial L}{\partial \mathbf{c}}, \mu)$  // Riemannian gradient update
end
return  $\mathbf{c}^* = \mathbf{c}^{(I)}$ 

```

testing. Running the optimization on the full-size reconstruction problem per sample is intractable because all projection images and the reconstructed volume need to reside on the GPU simultaneously which is beyond the memory capacity of recent consumer graphics boards. Hence, we subdivide each volume into 11 stacks of 100 slices which are reconstructed independently during optimization. This leads to a setting where only the central 1100 of 2014 slices of each scan are utilized. The outer slices are omitted because of an increasing influence of cone-beam artefacts. The described setting results in a training set of 55 individual samples from five different bone scans reconstructed per epoch for the full data set case. In the per-scan setting, all 11 stacks of the target scan are used during optimization. Algorithm 1 is valid for both experimental settings.

In addition to splitting the volumes into smaller stacks, we downsample the projection images angularly and spatially by a factor of 2 and the reconstructions by a factor of 2 in each direction. Hence, after downsampling, each sample has 50 slices and half the width and height of the proprietary reconstruction given in Table 1 during optimization. Experiments are performed with a degree of $N = 2$ and $N = 3$ for the polynomial in Equation (1), that is, with just two or three free parameters involved. Projection images as well as the geometry configuration are saved after all pre-processing steps including the conversion to line integral domain such that, during optimization, only the polynomial correction step and the back-projection module itself need to be evaluated (see Figure 3). Optimization is performed for 200 epochs in the per-scan experiments and for 40 epochs in the full data set experiments leading to an identical number of update steps for both cases. All experiments are performed with a learning rate of $\mu = 1 \times 10^{-9}$.

For evaluation, as we have no dedicated ground-truth reconstruction without cupping artefacts, we compare different uncorrected and corrected reconstructions obtained with the proposed reconstruction pipeline and the proprietary reconstruction obtained with the black-box scanner software. All evaluations are done on the central 100 slices of the scans on full resolution. Even though we enforce a constant norm on the polynomial coefficients, the average intensity in the reconstructions is not preserved by the proposed correction step. Furthermore, the intensity values of the proprietary reconstruction are on a completely different scale than those obtained with our reconstruction pipeline. Hence, for comparison purposes, each reconstruction is rescaled such that the background has a value of 0 and the bone has a value of 1800 which corresponds to the HU-value of cortical bone.⁴⁶ The histogram of each scan is computed and the grey values I_{bone} and $I_{\text{background}}$ corresponding to bone and background peak, respectively,

are identified. The rescaling is performed independently for each scan via

$$\hat{I}_j = \frac{I_j - I_{\text{background}}}{I_{\text{bone}} - I_{\text{background}}} * 1800\text{HU} \quad (4)$$

for I_j being the original grey value of the j th reconstructed voxel and \hat{I}_j being the rescaled grey value of that voxel in Hounsfield Units. For quantification of the cupping artefacts, we compute the outer and inner contour of the bone per slice using morphological snakes.⁴⁷ These contours are used to programmatically and repeatedly extract 100 lines per slice across the bone connecting the outer and inner contour at equally spaced points. Profiles of the bone grey values are evaluated along these lines. Furthermore, the middle points between corresponding points on the outer and the inner contour are used to define a middle contour which splits the bone into an inner and outer area per slice.

4 | RESULTS

Figure 4 shows the centre slices of three different murine tibia reconstructions. A visual comparison of our reconstruction to the proprietary reconstruction ('Ours uncorrected' and 'Proprietary') proves high accordance with clearly visible small-scale structures inside the cortical bone. The resulting polynomial coefficients for correction are $\mathbf{c}_{N=2} = (0.813, 0.582)$ and $\mathbf{c}_{N=3} = (0.815, 0.576, 0.063)$ for the full data set experiment and $\mathbf{c}_{N=2} = (0.855, 0.519)$ and $\mathbf{c}_{N=3} = (0.854, 0.519, 0.037)$ for a per-scan experiment. Both the uncorrected and the proprietary reconstruction exhibit decreasing grey values from the outer part of the bone towards the bone marrow. In the corrected versions of the reconstruction obtained with the presented pipeline, the grey values of the bone tissue are more homogeneous across the bone. These observations hold for the per-scan optimization (Figure 4, upper row) as well as for the full data set experiments (Figure 4, rows two and three). No clear visual difference can be observed between a correction with degree $N = 2$ and $N = 3$ (Figure 4, columns four and five). Figures 5A–C visualize average profiles of bone grey values across the bone, that is, along lines connecting the outer and the inner bone contour as described in Section 3. Both the proprietary and our uncorrected pipeline have line profiles with a negative slope representing decreasing grey values from outer to inner contour. In addition, both test samples from the full data set experiments exhibit extraordinarily high grey values close to the outer bone contour which are slightly more pronounced in the uncorrected reconstruction obtained with our pipeline than in the proprietary one. Apart from that, uncorrected and proprietary reconstruction show a similar trend in

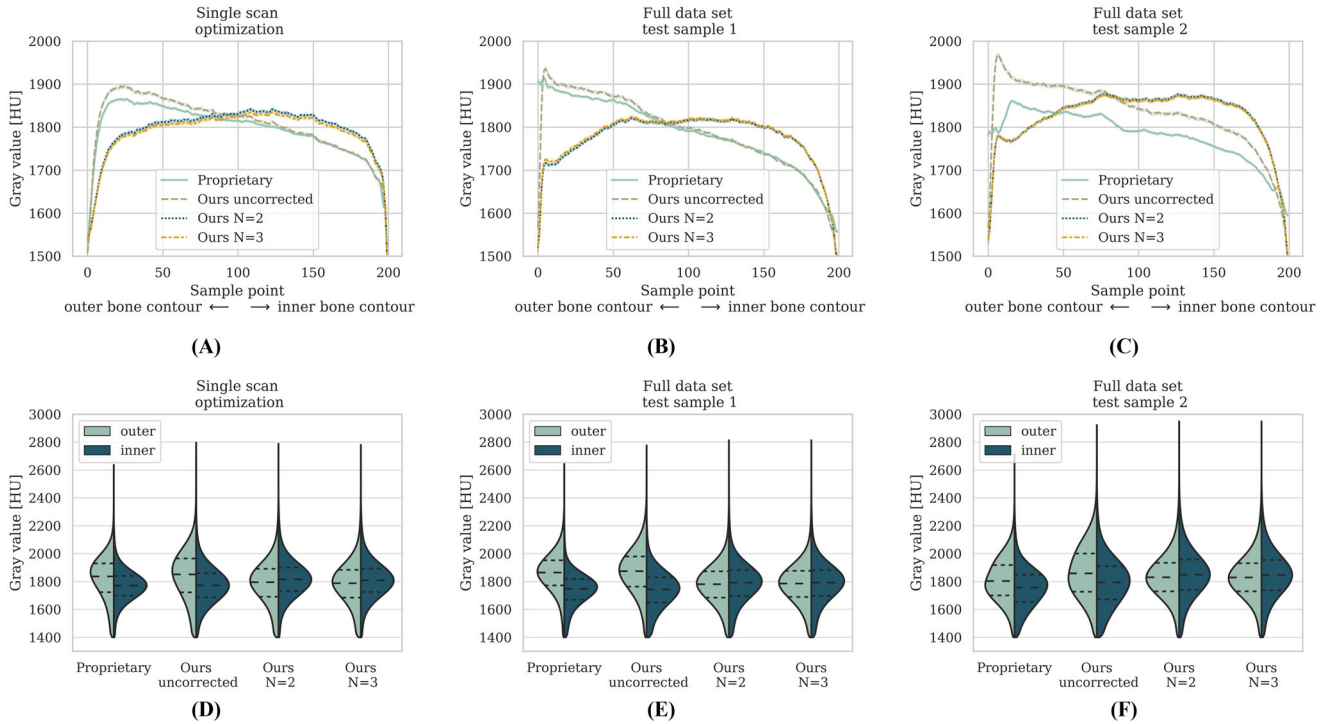


FIG 5 Upper row: Average line profiles connecting outer and inner bone contours. Proprietary and uncorrected reconstructions exhibit peaks close to the outer contour and decreasing grey values towards the inner contour. Grey values remain largely constant in both corrected versions with some drop off towards both outer and inner contour. The standard deviation across different lines connecting outer and inner bone and different slices is in the range of the line width. Lower row: The kernel density estimation of bone grey values (kernel bandwidth: 0.1σ , σ : standard variance of grey values) computed inside the outer and inner region of the bone. Quartiles are indicated by dashed lines for different reconstructions. The proposed correction aligns outer and inner grey values when using a polynomial of degree $N = 2$ and $N = 3$. Note that we have excluded all grey values below 1400 HU because these correspond to cavities inside the bone which are not distributed equally across the bone and would distort the results. Panels A and D correspond to the per-scan experiment and Panels B, C, E and F depict the two test samples in the full data set experiment

TABLE 2 All quantitative results are given in the following format: per-scan experiment, full data set test sample 1, full data set test sample 2. The best result for each metric is highlighted in bold font

	Proprietary	Ours uncorrected	Ours $N = 2$	Ours $N = 3$
s	-0.622, -1.341, -0.851	-0.755, -1.386, -1.095	0.172, -0.124, 0.006	0.165, -0.154, -0.001
Δg [HU]	69.53, 105.49, 42.45	80.03, 112.96, 57.19	6.24, 8.79, 19.40	5.73 , 6.69, 18.31

Note We compute the slope s of a straight line fitted to average grey value profiles along lines connecting outer and inner contour and the mean absolute grey value offset between outer and inner bone region Δg in HU. For both metrics, we regard values close to 0 as best.

their average line profiles. Similarly, there is no apparent difference in the line profiles of the corrected reconstructions with $N = 2$ or $N = 3$. Compared to the uncorrected reconstruction, however, the line profiles of the corrected reconstruction do not show the decreasing behaviour. Instead, they remain largely constant with a slight drop-off towards both sides. This is also reflected in the quantitative metrics in Table 2. We fit a straight line to each average line profile and report its slope s to measure the decrease or increase of grey values between inner and outer contour. The uncorrected reconstruction obtained with our proposed pipeline has the largest negative slope followed by the proprietary reconstruction. For the corrected versions,

the slope is closer to zero. It is even slightly positive for the per-scan experiment, still slightly negative for the first full data experiment test sample and almost perfectly zero for the second test sample. Figure 5D-F visualizes the distribution of bone grey values in the outer and inner bone regions of all 100 central slices at full resolution with quartiles indicated by dashed lines for the proprietary, uncorrected and both corrected reconstructions. For the uncorrected case, the inner and outer distributions exhibit a clear vertical offset with grey values being lower in the inner section of the bone. This difference is reduced in both corrected reconstructions. The quantitative absolute difference in mean grey values between the outer and inner part Δg can

be found in Table 2. Again, it is highest for our uncorrected reconstruction, followed by the proprietary reconstruction and with best results for the two corrected versions. In the best case (test sample 1), a mean difference of 112.96 HU over all slices in the uncorrected reconstruction is reduced to 6.69 HU after correction with $N = 3$ which is a reduction by 94%. Even in the worst case, a mean grey value difference of 57.19 HU is reduced to 18.31 HU which still corresponds to a reduction by 68%.

5 | DISCUSSION

The presented pipeline fits the coefficients \mathbf{c} of a polynomial operating in projection domain using a straightforward, self-supervised target function defined on the reconstructed volume. This allows for a data-driven, retrospective calibration for cupping correction without the need to acquire any extra calibration measurements or to manually set up an entire optimization algorithm. With this, even though our reconstruction pipeline is deep learning compatible, we do not perform deep learning in the classical sense of fitting a highly overparametrized neural network but use the built-in automatic differentiation of *PyTorch* to perform gradient-based optimization on a problem that would be very hard to set up and derive with respect to the free parameters otherwise. Extending that algorithm with deep networks is easily implemented by attaching the deep model to the computational graph during the forward pass. The general optimization procedure remains identical. Experiments have been performed with a polynomial of orders 2 and 3 which have both yielded improved reconstructions over the uncorrected one. On the used data set, both versions yield very similar results and we cannot decide which one performs better. Conveniently, the fitted polynomial operates on the projection images' intensity values only. Therefore, it is largely independent of the resolution of both projection images and reconstruction volume. We exploit this property by running the optimization on downsampled data for computational reasons, but we use the resulting polynomial for correction of the full resolution data. The beam-hardening correction is not intensity-preserving by itself because the TV norm does not punish piecewise constant offsets in the data. As the data used here stems from an uncalibrated scanner, the absolute grey values are not directly physically interpretable. Hence, intensity preservation is not a primary concern but can be achieved by a subsequent rescaling (see Equation 4). This process can easily be automated and applied to many samples in order to obtain consistent grey values even if optimization is performed per sample. In the case of a large series of samples with very similar properties, an optimization procedure comparable to the described full data set experiment would be preferable. A representative training set can be used to

calibrate the parameters \mathbf{c} which are then applied to all samples of the series without changes. In our experiments, the per sample and the full data set setup yielded similar coefficients \mathbf{c} . Hence, we expect similar cupping correction performance for both methods as long as the samples in the data set have comparable absorption properties. Convergence curves in the [supplementary material](#) indicate that both experimental settings converge.

The self-supervised fit of coefficients is easy to apply but has some limitations. It can potentially converge towards physically implausible results if the hyperparameters such as the learning rate are not controlled carefully. This can be counteracted by introducing further constraints such as monotonicity and convexity of the polynomial.⁴⁸ However, *PyTorch* and comparable deep learning frameworks are primarily designed for unconstrained optimization of highly parametrized models and might not be perfectly suited for strongly constrained settings. Currently, the unit ℓ_2 -norm for the free parameters \mathbf{c} is enforced by using a special Riemannian optimizer. Hence, additional constraints are not easily added because they directly affect the optimizer itself. If artefact-reduced ground-truth reconstructions are available, they can be used to drive the training in a supervised manner to avoid physically implausible results as well as intensity shifts. This would also make the requirement of any additional norm obsolete. Furthermore, we have not performed a detailed evaluation of the influence of different noise levels in the reconstruction on our algorithm. The TV norm is frequently utilized for denoising applications as well. Noise reduction techniques, however, usually rely on averaging operations over neighbourhood pixels. As our method is restricted to the same polynomial per-pixel mapping for the entire stack of projection images, such a neighbourhood-dependent operation is not possible by design. Hence, in our case, the minimization of the TV norm needs to be achieved by cupping correction rather than noise reduction. It has already been demonstrated that incorporating a denoiser based on supervised learning into the proposed pipeline yields state-of-the-art results.⁴⁹ Investigating a joint denoising and cupping correction approach can be an interesting avenue for future work.

Overall, the presented work on retrospective cupping correction is a simple example which expresses the value of a differentiable reconstruction algorithm. While comparable experiments incorporating differentiable CT reconstruction have already shown its usefulness on simulated data,^{25,50} it has not yet been applied extensively to real data. This paper demonstrates the applicability to a real-world example and opens up many possibilities to leverage the idea in future work. We plan to investigate the use of the proposed pipeline for purposes such as denoising or other artefact reduction aiming at the development of an XRM scanning protocol suitable for in vivo imaging. While we

work on XRM data here, the general idea of differentiable reconstruction is not limited to a specific scanner but can be generalized to any flat-panel CBCT device.

6 | CONCLUSIONS

We present a complete reconstruction algorithm for Zeiss X-ray microscopes for which, to the best of our knowledge, no other open-source algorithm exists at the time of writing. With the back-projection step of this pipeline being differentiable, a cupping correction can be retrospectively calibrated from real XRM data. This relaxes the dependency on proprietary software and opens the door for further applications of learned modules in conjunction with XRM reconstruction. Ultimately, such algorithms can help to overcome some of the challenges associated with high-resolution *in vivo* bone imaging using XRM.

ACKNOWLEDGEMENTS

The research leading to these results has received funding from the European Research Council (ERC) under the European Union's Horizon 2020 research and innovation program (ERC Grant No. 810316).

Open access funding enabled and organized by Projekt DEAL.

CONFLICT OF INTEREST

The authors declare that there is no conflict of interest that could be perceived as prejudicing the impartiality of the research reported.

ORCID

Mareike Thies  <https://orcid.org/0000-0002-1364-4337>

REFERENCES

- Gruber, R., Pietschmann, P., & Peterlik, M. (2008). Introduction to bone development, remodelling and repair. In *Radiology of osteoporosis* (pp. 1–23). Springer Berlin Heidelberg.
- Buenzli, P. R., & Sims, N. A. (2015). Quantifying the osteocyte network in the human skeleton. *Bone*, *75*, 144–150.
- Hannah, K. M., Thomas, C. D., Clement, J. G., De Carlo, F., & Peele, A. G. (2010). Bimodal distribution of osteocyte lacunar size in the human femoral cortex as revealed by micro-CT. *Bone*, *47*(5), 866–871.
- Grüneboom, A., Hawwari, I., Weidner, D., Culemann, S., Müller, S., Henneberg, S., Brenzel, A., Merz, S., Bornemann, L., Zec, K., Wuelling, M., Kling, L., Hasenberg, M., Voortmann, S., Lang, S., Baum, W., Ohs, A., Kraff, O., Quick, H. H., ... Gunzer, M. (2019). A network of trans-cortical capillaries as mainstay for blood circulation in long bones. *Nature Metabolism*, *1*(2), 236–250.
- Rho, J.-Y., Kuhn-Spearing, L., & Zioupos, P. (1998). Mechanical properties and the hierarchical structure of bone. *Medical Engineering and Physics*, *20*(2), 92–102.
- Grüneboom, A., Kling, L., Christiansen, S., Mill, L., Maier, A., Engelke, K., Quick, H. H., Schett, G., & Gunzer, M. (2019). Next-generation imaging of the skeletal system and its blood supply. *Nature Reviews Rheumatology*, *15*(9), 533–549.
- Yu, B., Pacureanu, A., Olivier, C., Cloetens, P., & Peyrin, F. (2021). Quantification of the bone lacunocanicular network from 3D X-ray phase nanotomography images. *Journal of Microscopy*, *282*(1), 30–44.
- Varga, P., Hesse, B., Langer, M., Schrof, S., Männicke, N., Suhonen, H., Pacureanu, A., Pahr, D., Peyrin, F., & Raum, K. (2015). Synchrotron X-ray phase nano-tomography-based analysis of the lacunar–canicular network morphology and its relation to the strains experienced by osteocytes *in situ* as predicted by case-specific finite element analysis. *Biomechanics and Modeling in Mechanobiology*, *14*(2), 267–282.
- Kerschnitzki, M., Kollmannsberger, P., Burghammer, M., Duda, G. N., Weinkamer, R., Wagermaier, W., & Fratzl, P. (2013). Architecture of the osteocyte network correlates with bone material quality. *Journal of Bone and Mineral Research*, *28*(8), 1837–1845.
- Clark, D. P., & Badea, C. (2014). Micro-CT of rodents: State-of-the-art and future perspectives. *Physica Medica*, *30*(6), 619–634.
- Longo, A. B., Salmon, P. L., & Ward, W. E. (2017). Comparison of *ex vivo* and *in vivo* micro-computed tomography of rat tibia at different scanning settings. *Journal of Orthopaedic Research*, *35*(8), 1690–1698.
- Mill, L., Bier, B., Syben, C., Kling, L., Klingberg, A., Christiansen, S., Schett, G., & Maier, A. (2018). Towards *in-vivo* x-ray nanoscopy—The effect of motion on image quality. In *Bildverarbeitung für die Medizin 2018* (pp. 115–120). Springer Berlin Heidelberg.
- Huang, Y., Mill, L., Stoll, R., Kling, L., Aust, O., Wagner, F., Grüneboom, A., Schett, G., Christiansen, S., & Maier, A. (2021). Semi-permeable filters for interior region of interest dose reduction in X-ray microscopy. In *Bildverarbeitung für die Medizin 2021* (pp. 61–66). Springer Fachmedien Wiesbaden.
- Ghani, M. U., & Karl, W. (2018). Deep learning based sinogram correction for metal artifact reduction. *Electronic Imaging*, *2018*(15), 4721–4728.
- Ketcha, M. D., Marrama, M., Souza, A., Uneri, A., Wu, P., Zhang, X., Helm, P. A., & Siewerdsen, J. H. (2021). Sinogram + image domain neural network approach for metal artifact reduction in low-dose cone-beam computed tomography. *Journal of Medical Imaging*, *8*(5), 1–16.
- Yi, X., & Babyn, P. (2018). Sharpness-aware low-dose CT denoising using conditional generative adversarial network. *Journal of Digital Imaging*, *31*(5), 655–669.
- Patwari, M., Gutjahr, R., Raupach, R., & Maier, A. (2020). JBFnet - Low dose CT denoising by trainable joint bilateral filtering. In *Proc. MICCAI* (pp. 506–515). Springer.
- Jacobsen, C. (2019). *X-ray microscopy*. Advances in Microscopy and Microanalysis. Cambridge University Press.
- Niverty, S., Torbatissaraf, H., Nikitin, V., De Andrade, V., Niazorau, S., Kublik, N., Azeredo, B., Tekawade, A., De Carlo, F., & Chawla, N. (2021). Computational imaging in 3D X-ray microscopy: Reconstruction, image segmentation and time-evolved experiments. In *IEEE International Conference on Image Processing* (pp. 3502–3506). IEEE.
- Langer, M., & Peyrin, F. (2016). 3D X-ray ultra-microscopy of bone tissue. *Osteoporosis International*, *27*(2), 441–455.
- Andrews, J. C., Almeida, E., van der Meulen, M. C. H., Alwood, J. S., Lee, C., Liu, Y., Chen, J., Meirer, F., Feser, M., Gelb, J., Rudati, J., Tkachuk, A., Yun, W., & Pianetta, P. (2010). Nanoscale

- x-ray microscopic imaging of mammalian mineralized tissue. *Journal of Microscopy and Microanalysis*, 16(3), 327–336.
22. Feldkamp, L. A., Davis, L. C., & Kress, J. W. (1984). Practical cone-beam algorithm. *Journal of the Optical Society of America A*, 1(6), 612–619.
 23. Zeng, G. L. (2010). *Medical image reconstruction: A conceptual tutorial*. Springer.
 24. Parker, D. L. (1982). Optimal short scan convolution reconstruction for fan beam CT. *Medical Physics*, 9(2), 254–257.
 25. Maier, A., Syben, C., Stimpel, B., Würfl, T., Hoffmann, M., Schebesch, F., Fu, W., Mill, L., Kling, L., & Christiansen, S. (2019). Learning with known operators reduces maximum error bounds. *Nature Machine Intelligence*, 1(8), 373–380.
 26. Öktem, O., Adler, J., & Kohr, H. (2022). Operator discretization library (ODL). GitHub. Retrieved from <https://github.com/odlgroup/odl>
 27. van Aarle, W., Palenstijn, W. J., Cant, J., Janssens, E., Bleichrodt, F., Dabravolski, A., Beenhouwer, J. D., Batenburg, K. J., & Sijbers, J. (2016). Fast and flexible X-ray tomography using the ASTRA toolbox. *Optics Express*, 24(22), 25129–25147.
 28. Gürsoy, D., De Carlo, F., Xiao, X., & Jacobsen, C. (2014). TomoPy: A framework for the analysis of synchrotron tomographic data. *Journal of Synchrotron Radiation*, 21.
 29. Syben, C., Michen, M., Stimpel, B., Seitz, S., Ploner, S., & Maier, A. K. (2019). PYRO-NN: Python reconstruction operators in neural networks. *Medical Physics*, 46(11), 5110–5115.
 30. Ronchetti, M. (2020). TorchRadon: Fast differentiable routines for computed tomography. *arxiv*.
 31. Paszke, A., Gross, S., Massa, F., Lerer, A., Bradbury, J., Chanan, G., Killeen, T., Lin, Z., Gimelshein, N., Antiga, L., Desmaison, A., Kopf, A., Yang, E., DeVito, Z., Raison, M., Tejani, A., Chilamkurthy, S., Steiner, B., Fang, L., ... Chintala, S. (2019). PyTorch: An imperative style, high-performance deep learning library. In *Proc. NeurIPS* (pp. 8024–8035). Curran Associates, Inc.
 32. Yang, X. (2021). *Practical basics and applications of X-ray tomography* (pp. 27–44). Springer.
 33. Yang, X., & Schroer, C. (2021). Strategies of deep learning for tomographic reconstruction. In *IEEE International Conference on Image Processing* (pp. 3473–3476).
 34. Huang, Y., Wang, S., Guan, Y., & Maier, A. (2020). Limited angle tomography for transmission X-ray microscopy using deep learning. *Journal of Synchrotron Radiation*, 27(2), 477–485.
 35. Chen, H., Zhang, Y., Chen, Y., Zhang, J., Zhang, W., Sun, H., Lv, Y., Liao, P., Zhou, J., & Wang, G. (2018). LEARN: Learned experts' assessment-based reconstruction network for sparse-data CT. *IEEE Transactions on Medical Imaging*, 37(6), 1333–1347.
 36. Würfl, T., Hoffmann, M., Christlein, V., Breining, K., Huang, Y., Unberath, M., & Maier, A. K. (2018). Deep learning computed tomography: Learning projection-domain weights from image domain in limited angle problems. *IEEE Transactions on Medical Imaging*, 37(6), 1454–1463.
 37. Lagerwerf, M. J., Pelt, D. M., Palenstijn, W. J., & Batenburg, K. J. (2020). A computationally efficient reconstruction algorithm for circular cone-beam computed tomography using shallow neural networks. *Journal of Imaging*, 6(12), 135.
 38. De Carlo, F., Gürsoy, D., Marone, F., Rivers, M., Parkinson, D. Y., Khan, F., Schwarz, N., Vine, D. J., Vogt, S., Gleber, S.-C., Narayanan, S., Newville, M., Lanzirrotti, T., Sun, Y., Hong, Y. P., & Jacobsen, C. (2014). Scientific data exchange: A schema for HDF5-based storage of raw and analyzed data. *Journal of Synchrotron Radiation*, 21(6), 1224–1230.
 39. Brooks, R. A. (1977). A quantitative theory of the Hounsfield unit and its application to dual energy scanning. *Journal of Computer Assisted Tomography*, 1(4), 487–493.
 40. Schulze, R., Heil, U., Groß, D., Bruellmann, D. D., Dranischnikow, E., Schwanecke, U., & Schoemer, E. (2011). Artefacts in CBCT: A review. *Dentomaxillofacial Radiology*, 40(5), 265–273.
 41. Brooks, R. A., & Di Chiro, G. (1976). Beam hardening in x-ray reconstructive tomography. *Physics in Medicine and Biology*, 21(3), 390–398.
 42. Kachelrieß, M., Sourbelle, K., & Kalender, W. A. (2006). Empirical cupping correction: A first-order raw data pre-correction for cone-beam computed tomography. *Medical Physics*, 33(5), 1269–1274.
 43. Würfl, T., Maaß, N., Dennerlein, F., Huang, X., & Maier, A. K. (2017). Epipolar consistency guided beam hardening reduction-ECC². In *Proc. Fully3D* (pp. 181–185).
 44. Kochurov, M., Karimov, R., & Kozlukov, S. (2020). Geopt: Riemannian optimization in PyTorch. *arxiv*.
 45. Bécigneul, G., & Ganeva, O.-E. (2019). Riemannian adaptive optimization methods. *arxiv*.
 46. Fat, D. L., Kennedy, J., Galvin, R., O'Brien, F., Mc Grath, F., & Mullett, H. (2012). The Hounsfield value for cortical bone geometry in the proximal Humerus: an in vitro study. *Skeletal Radiology*, 41(5), 557–568.
 47. Márquez-Neila, P., Baumela, L., & Alvarez, L. (2014). A morphological approach to curvature-based evolution of curves and surfaces. *IEEE Transactions on Pattern Analysis and Machine Intelligence*, 36(1), 2–17.
 48. Würfl, T., Maaß, N., Dennerlein, F., Aichert, A., & Maier, A. (2018). Physical constraints for beam hardening reduction using polynomial models. In *Proc. CT-Meeting* (pp. 356–359).
 49. Wagner, F., Thies, M., Gu, M., Huang, Y., Pechmann, S., Patwari, M., Ploner, S., Aust, O., Uderhardt, S., Schett, G., Christiansen, S., & Maier, A. (2022). Ultra low-parameter denoising: Trainable bilateral filter layers in computed tomography. *arxiv*.
 50. Syben, C., Stimpel, B., Lommen, J., Würfl, T., Dörfler, A., & Maier, A. (2018). Deriving neural network architectures using precision learning: Parallel-to-fan beam conversion. In *German Conference on Pattern Recognition* (pp. 503–517). Springer.

SUPPORTING INFORMATION

Additional supporting information can be found online in the Supporting Information section at the end of this article.

How to cite this article: Thies, M., Wagner, F., Huang, Y., Gu, M., Kling, L., Pechmann, S., Aust, O., Grüneboom, A., Schett, G., Christiansen, S., & Maier, A. (2022). Calibration by differentiation – Self-supervised calibration for X-ray microscopy using a differentiable cone-beam reconstruction operator. *Journal of Microscopy*, 287, 81–92. <https://doi.org/10.1111/jmi.13125>